ORIGINAL RESEARCH • NEURORADIOLOGY

Radiology

Brain MRI with Quantitative Susceptibility Mapping: Relationship to CT Attenuation Values

Sonoko Oshima, MD • Yasutaka Fushimi, MD, PhD • Tomohisa Okada, MD, PhD • Kyoko Takakura, RT • Chunlei Liu, PhD • Yusuke Yokota, MD • Yoshiki Arakawa, MD, PhD • Nobukatsu Sawamoto, MD, PhD • Susumu Miyamoto, MD, PhD • Kaori Togashi, MD, PhD

From the Department of Diagnostic Imaging and Nuclear Medicine (S.O., Y.F., K. Takakura, Y.Y., K. Togashi), Human Brain Research Center (T.O.), Department of Neurosurgery (Y.A., S.M.), and Department of Human Health Sciences (N.S.), Graduate School of Medicine, Kyoto University, 54 Shogoin Kawahara-cho, Sakyo-ku, Kyoto, 606-8507 Japan; and Department of Electrical Engineering and Computer Sciences and Helen Wills Neuroscience Institute, University of California, Berkeley, Calif (C.L.). Received December 25, 2018; revision requested April 17, 2019; revision received October 1; accepted November 5. **Address correspondence to** Y.F. (e-mail: *yfushimi@kuhp.kyoto-u.ac.jp*).

This work was supported by Japan Society for the Promotion of Science KAKENHI (grant JP18K07711) and the Kyoto University Foundation.

Conflicts of interest are listed at the end of this article.

Radiology 2020; 294:600–609 • https://doi.org/10.1148/radiol.2019182934 • Content codes: NR MR

Background: Quantitative susceptibility mapping (QSM) is used to differentiate between calcification and iron deposits. Few studies have examined the relationship between CT attenuation values and magnetic susceptibility in such materials.

Purpose: To assess the relationship among metal concentration, CT attenuation values, and magnetic susceptibility in paramagnetic and diamagnetic phantoms, and the relationship between CT attenuation values and susceptibility in brain structures that have paramagnetic or diamagnetic properties.

Materials and Methods: In this retrospective study, CT and MRI with QSM were performed in gadolinium and calcium phantoms, patients, and healthy volunteers between June 2016 and September 2017. In the phantom study, we evaluated correlations among metal concentration, CT attenuation values, and susceptibility. In the human study, Pearson and Spearman correlations were performed to assess the relationship between CT attenuation values and susceptibility in regions of interest placed in the globus pallidus (GP), putamen, caudate nucleus, substantia nigra, red nucleus, dentate nucleus, choroid plexus, and hemorrhagic and calcified lesions.

Results: Eighty-four patients (mean age, 64.8 years ± 19.6; 49 women) and 20 healthy volunteers (mean age, 72.0 years ± 7.6; 11 men) were evaluated. In the phantoms, strong linear correlations were identified between gadolinium concentration and CT and MRI QSM values (R^2 = 0.95 and 0.99, respectively; $P < .001$ for both) and between calcium concentration and CT and MRI QSM values (R^2 = 0.89 [$P = .005$] and R^2 = 0.98 [$P < .001$], respectively). In human studies, positive correlations between CT attenuation values and susceptibility were observed in the GP (R^2 = 0.52, $P < .001$) and in hemorrhagic lesions (R^2 = 0.38, $P < .001$), and negative correlations were found in the choroid plexus (R^2 = 0.53, $P < .001$) and in calcified lesions (R^2 = 0.38, $P = .009$).

Conclusion: CT attenuation values showed a positive correlation with susceptibility in the globus pallidus and hemorrhagic lesions and negative correlation in the choroid plexus and calcified lesions.

Online supplemental material is available for this article.

CT has been widely used for depicting conditions such as calcification and hemorrhage. CT attenuation values measured in Hounsfield units are determined by the relationship of the linear attenuation coefficient of a pixel to that of water. The attenuation of acute hemorrhage at CT is typically within the range of 50–100 HU, whereas the attenuation of calcification is usually more than 100 HU (1). However, an overlap exists in the CT attenuation values of blood and calcium at less than 100 HU (2).

Compared with CT, MRI shows higher contrast of the brain parenchyma, and its role in evaluating such tissues is growing. Susceptibility-weighted imaging is sensitive to materials that generate a phase shift in gradient-echo MRI data, such as iron deposits, hemorrhage, and calcification. However, it cannot help differentiate between paramagnetic and diamagnetic substances (3). The MRI technique of quantitative susceptibility mapping (QSM) uses phase data (4–9) to provide quantitative values of magnetic susceptibility, which allows differentiation of paramagnetic materials (eg, iron and hemorrhage) from diamagnetic materials (eg, calcification).

A previous study showed a strong correlation between magnetic susceptibility and the concentration of gadolinium (10). Susceptibility also correlated well with the concentration of iron in phantoms (11), deep gray matter (7,12,13), and hemorrhage (14,15). However, few studies have examined the relationship between CT attenuation values and susceptibility in intracranial areas that contain paramagnetic materials such as iron and diamagnetic materials such as calcification. Paramagnetic mineralization is observed in the deep gray nuclei, most strongly in the globus pallidus (GP) (13,16). In contrast, the choroid plexus commonly contains calcification, which is diamagnetic (17).

Abbreviations

GP = globus pallidus, QSM = quantitative susceptibility mapping, ROI = region of interest

Summary

Susceptibility in the globus pallidus, choroid plexus, and hemorrhagic and calcified lesions correlated with CT attenuation values, suggesting the possibility of estimating CT attenuation values from quantitative susceptibility mapping.

Key Results

- The globus pallidus showed a positive correlation between maximum CT attenuation values and maximum magnetic susceptibility (R^2 = 0.52, $P < .001$).
- Negative correlations between maximum CT attenuation values and minimum magnetic susceptibility were observed in the choroid plexus (R^2 = 0.53, $P < .001$) and in calcified lesions (R^2 = 0.38, P = .009) owing to the high CT attenuation values and negative susceptibility of calcium deposits.
- There was no relationship between CT attenuation values and magnetic susceptibility in the putamen, caudate nucleus, red nucleus, substantia nigra, or dentate nucleus; this suggests that iron deposition and calcification in these regions are low.

The aims of this study were to assess *(a)* the relationship among metal concentration, CT attenuation values, and susceptibility in paramagnetic and diamagnetic phantoms and *(b)* the relationship between CT attenuation values and magnetic susceptibility in normal paramagnetic and diamagnetic structures of the brain, including the deep gray matter and choroid plexus, and hemorrhagic and calcified lesions.

Materials and Methods

This retrospective study was approved by the institutional ethics committee. Written informed consent was obtained from the healthy volunteers. The requirement to obtain written informed consent was waived for patients.

Phantoms

We constructed gadolinium and calcium carbonate ($CaCO_3$) phantoms as follows. We fixed 2% agarose gel (Wakenyaku, Kyoto, Japan) in spherical form (diameter, 2.5 cm) with various concentrations of gadoterate meglumine (Dotarem; Guerbet, Villepinte, France) and $CaCO_3$ in a container filled with water (Fig 1a). The concentrations of gadolinium were 0, 1.0, 2.0, 3.0, 4.0, and 5.0 mmol/L, and the concentrations of $CaCO_3$ were 0, 1.0, 2.0, 3.0, 4.0, and 5.0 mol/L.

Patients and Volunteers

Twenty healthy volunteers older than 60 years underwent both low-dose CT (volume CT dose index, 40 mGy; dose-length product, 720 mGy/cm) and MRI with a three-dimensional gradient-echo sequence. We retrospectively included 147 patients who had undergone MRI, including a three-dimensional gradient-echo sequence, and CT of the brain at our hospital from June 14, 2016, to September 25, 2017. Sixty-three patients were excluded: 58 because the interval between CT and QSM was longer than 1 year and five because image quality was poor due to large lesions such as hematoma. In total, 104 patients and volunteers were included in the analysis. The mean interval (± standard deviation) between CT and QSM was 55.4 days ± 84.5 (range, 0–355 days).

Image Acquisition and Postimaging Procedure

Nonenhanced CT and MRI scans were obtained. QSM was calculated by using software provided for research (STI Suite, version 2.2; Medical Imaging, Brain Imaging and Cell Modulation, University of California, Berkeley, Berkeley, Calif) (7). CT and QSM images were coregistered to each other. Details of the CT and MRI procedures are provided in Appendix E1 (online).

Region of Interest Analysis in the Phantom Study

A board-certified neuroradiologist (S.O., with 9 years of experience) manually placed circular regions of interest (ROIs) on the CT and QSM images of the gadolinium and $CaCO_3$ phantoms so that the ROIs covered the gadolinuim- and $CaCO_3$-doped gels. Susceptibility values were measured for each ROI and mean values were calculated. Correlations between metal concentration and CT attenuation values and between concentration and susceptibility were determined.

ROI Analysis in the Human Study

Two board-certified neuroradiologists (S.O. and Y.F., with 20 years of experience) placed ROIs on the center slice of the QSM images, in consensus, in each of the following regions: GP, putamen, caudate nucleus, substantia nigra, red nucleus, dentate nucleus, and the low-signal-intensity region of the choroid plexus. The positions of the ROIs were then applied to the CT images from the same patient or volunteer by using open-source software (ImageJ, version 1.50; National Institutes of Health, Bethesda, Md). We also placed ROIs on hemorrhagic and calcified lesions with reference to the CT and MRI scans (including QSM, T1-weighted, T2-weighted, and T2*-weighted images) and the clinical information. When diamagnetic lesions were surrounded by paramagnetic areas, we preferentially chose the inner diamagnetic (calcified) parts for ROI placement. For each patient with lesions, up to three lesions were selected for ROI placement.

Mean CT attenuation value and mean QSM value (magnetic susceptibility) were calculated for each ROI. When mean QSM value was positive (paramagnetic ROIs), the maximum and 95th percentile CT attenuation values and maximum and 95th percentile QSM values were also calculated to better understand the characteristics of the CT attenuation values and susceptibility, as is commonly adopted in the analysis of apparent diffusion coefficients (18). For ROIs with mean QSM values showing negative values (diamagnetic ROIs), the maximum and 95th percentile CT attenuation values and the minimum and fifth percentile QSM values were calculated instead. Correlations between CT attenuation values and susceptibility were assessed between the following pairs: mean CT attenuation value and mean QSM value, maximum CT attenuation value and maximum QSM value, and 95th percentile CT attenuation value and 95th percentile QSM value for paramagnetic ROIs and mean CT attenuation value and mean QSM value, maximum CT attenuation value and minimum QSM value, and 95th percentile CT attenuation value and fifth percentile QSM value for diamagnetic ROIs.

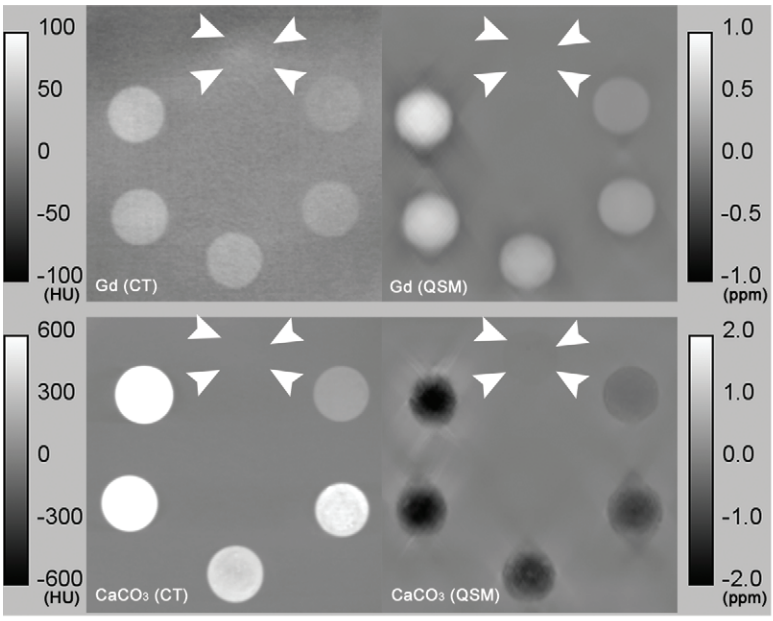

Figure 1: **(a)** CT scans (left) and quantitative susceptibility mapping (QSM) images (right) of gadolinium (Gd) phantoms with concentrations of 0, 1.0, 2.0, 3.0, 4.0, and 5.0 mmol/L (upper row), and calcium carbonate ($CaCO_3$) phantoms with concentrations of 0, 1.0, 2.0, 3.0, 4.0, and 5.0 mol/L (lower row). Arrowheads indicate gadolinium phantom with concentration of 0 mmol/L and the $CaCO_3$ phantom with concentration of 0 mol/L. The subsequent concentrations follow in a clockwise manner. **(b)** Graphs show excellent correlation between concentration and CT attenuation value and between concentration and susceptibility in Gd and $CaCO_3$ phantoms. CT_{max} = maximum CT attenuation value, QSM_{max} = maximum QSM value, QSM_{min} = minimum QSM value.

a.

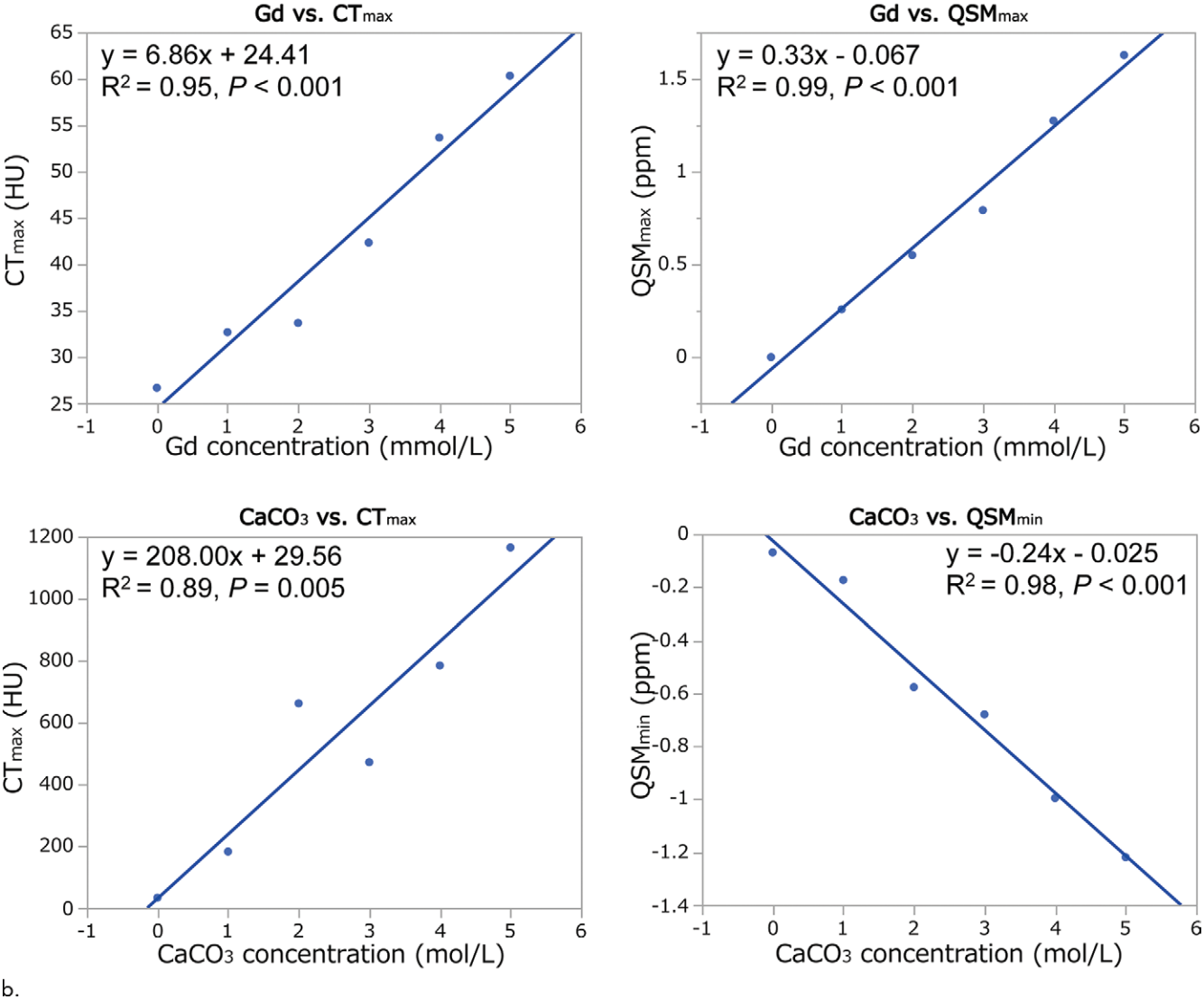

b.

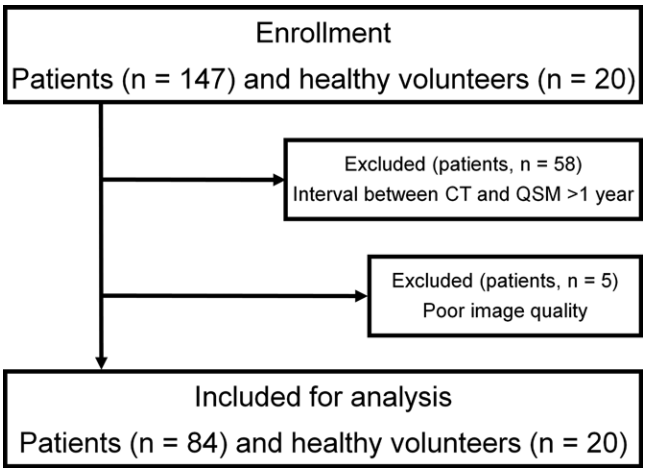

Figure 2: Flowchart shows patient and volunteer enrollment. QSM = quantitative susceptibility mapping.

We also evaluated correlations between CT and QSM for the group of 20 healthy volunteers.

Diagnostic Performance

One board-certified neuroradiologist (Y.Y., with 10 years of experience) differentiated calcified lesions from hemorrhagic lesions based on the CT images without QSM information.

Statistical Analysis

For the phantom study, we evaluated Pearson correlation coefficients between metal concentration and CT attenuation values and between metal concentration and magnetic susceptibility. For the human study, we assessed Pearson correlation coefficients with a linear regression method and Spearman rank correlation coefficients between CT attenuation values and susceptibility by using commercially available software (JMP, version 14.0; SAS Institute, Cary, NC). $P < .05$ was considered indicative of statistical significance. We also calculated correlation coefficients between CT attenuation values and susceptibility adjusted for age and interval between CT and MRI. Intraclass correlation coefficients to assess consistency between CT attenuation values and susceptibility were calculated with software (JMP, version 14.0) after normalization by using the *z* score of each value. We performed analyses for hemorrhagic and calcified lesions based on lesion-level data.

Coefficients of variation were also calculated for mean CT attenuation value, maximum or minimum CT attenuation value, 95th percentile or fifth percentile CT attenuation value, mean QSM value, maximum or minimum QSM value, and 95th percentile or fifth percentile QSM value in each ROI among patients, healthy volunteers, and the total cohort.

Results

Study Cohort Demographics

In the human study, a total of 104 patients and volunteers (mean age, 66.2 years ± 18.2; 58 women) were included in the analysis. There were 84 patients (mean age, 64.8 years ± 19.6; 49 women) and 20 healthy volunteers (mean age, 72.0 years ± 7.6; 11 men) (Fig 2). The characteristics of the patients and healthy volunteers are listed in Table 1.

Table 1: Characteristics of Patients and Volunteers

Characteristic	Value
Patients	
No. of patients	84
Mean age ± SD (y)	64.8 ± 19.6
Sex	
M	35
F	49
Underlying diseases	
Neurodegenerative disease	48
Intracranial neoplasm	22
Vascular malformation	5
Stroke	4
Aneurysm	1
Tuberous sclerosis	1
Hypopituitarism	1
Encephalomyelitis	1
Neuronal intranuclear inclusion disease	1
Healthy volunteers	
No. of volunteers	20
Mean age ± SD (y)	72.0 ± 7.6
Sex	
M	11
F	9

Note.—Except where indicated, data are numbers of patients or volunteers. SD = standard deviation.

Phantom Study

Gadolinium phantom.—We used six gadolinium phantoms. Linear regression analysis revealed positive correlations between gadolinium concentration and CT attenuation values (R^2 of mean, maximum, and 95th percentile CT attenuation values: 0.97, 0.95, and 0.98, respectively; $P < .001$) and between gadolinium concentration and susceptibility (R^2 of mean, maximum, and 95th percentile QSM values: 0.99, 0.99, and 0.98, respectively; $P < .001$).

$CaCO_3$ phantom.—We used six $CaCO_3$ phantoms. Linear regression analysis revealed a positive correlation between $CaCO_3$ concentration and CT attenuation values (R^2 of mean, maximum, and 95th percentile CT attenuation values: 0.90, 0.89, and 0.93, respectively; $P = .004$, .005, and .004) and a negative correlation between $CaCO_3$ concentration and susceptibility (R^2 of mean, minimum, and fifth percentile QSM values: 0.98, 0.98, and 0.93, respectively; $P < .001$) (Fig 1b).

Human Study

Figure 3 shows representative images of the ROIs. The areas of the ROIs are listed in Table E1 (online). Representative ex-

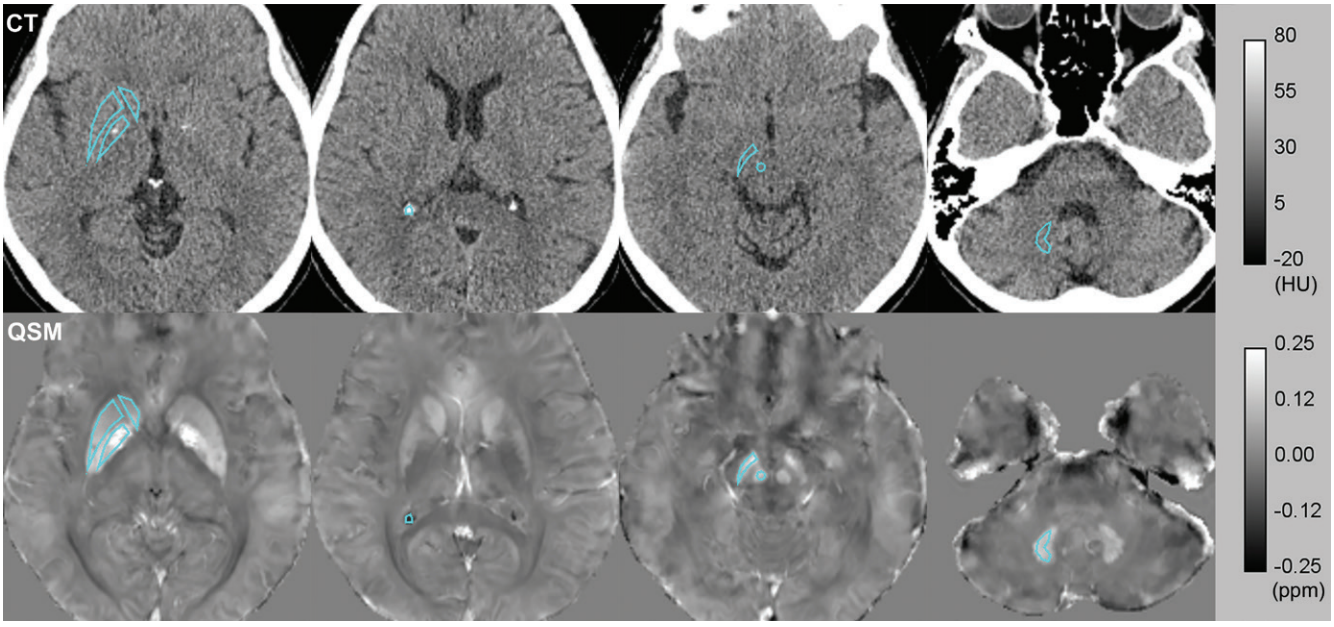

Figure 3: CT scans (top) and quantitative susceptibility mapping (QSM) images (bottom) show examples of regions of interest of normal structures (putamen, globus pallidus, caudate nucleus, choroid plexus, substantia nigra, red nucleus, and dentate nucleus). Note that CT and QSM images are coregistered to each other.

amples of CT and QSM images for healthy volunteers, a patient with anaplastic astrocytoma, and a patient with cavernous hemangioma are shown in Figures 4, 5, E1 (online), and E2 (online). In one patient, the right GP, putamen, and substantia nigra could not be assessed because of a large hematoma. The left dentate nucleus of another patient could not be assessed because of a large medulloblastoma. Pathologic lesions were found in 27 patients, nine of whom had multiple lesions. Forty-five pathologic lesions were identified, of which 28 were hemorrhagic. Of those 28 hemorrhagic lesions, 25 were chronic hemorrhage (≥1 month after onset) (chronic idiopathic intraparenchymal hemorrhage, n = 18; cavernous hemangioma, n = 6; and anaplastic oligodendroglioma, n = 1) and three were subacute hemorrhage (8 days to 1 month after onset) (metastatic tumor, n = 2; subacute idiopathic intraparenchymal hemorrhage, n = 1). Another 17 lesions were calcified and included calcifications in brain tumors (n = 12), subependymal tubers (n = 3), radiation-induced calcification (n = 1), and calcified aneurysm wall (n = 1). One hemorrhagic and two calcified lesions were confirmed at histopathologic examination.

Mean and standard deviations of CT attenuation values and susceptibility and R^2 for correlations between them are listed in Table 2. Mean susceptibility of the GP, putamen, caudate nucleus, red nucleus, substantia nigra, and dentate nucleus was positive, and that of the choroid plexus was negative. Figure 6a shows a scatter plot of maximum CT attenuation values and maximum or minimum susceptibility of all ROIs in phantoms, patients, and volunteers.

Linear regression analysis showed a positive correlation between CT attenuation values and susceptibility in the GP (R^2 of mean CT attenuation value and mean QSM value, maximum CT attenuation value and maximum QSM value, and 95th percentile CT attenuation value and 95th percentile QSM value: 0.30, 0.52, and 0.50, respectively; $P < .001$) (Figs 6b, E3 [online]; Table 2). A 23-year-old female patient showed markedly high CT attenuation values in the basal ganglia after chemoradiation therapy for a germ cell tumor (Fig E4 [online]). A negative correlation was seen in the choroid plexus (R^2 of mean CT attenuation value and mean QSM value, maximum CT attenuation value and minimum QSM value, and 95th percentile CT attenuation value and fifth percentile QSM value: 0.58, 0.53, and 0.56, respectively; $P < .001$) (Figs 6b, E3 [online]; Table 2).

Moderate to strong correlations were observed in hemorrhagic lesions (R^2 of mean CT attenuation value and mean QSM value, maximum CT attenuation value and maximum QSM value, and 95th percentile CT attenuation value and 95th percentile QSM value: 0.41, 0.38, and 0.38, respectively; $P < .001$) (Figs 6b, E3 [online]; Table 2) and calcified lesions (R^2 of maximum CT attenuation value and minimum QSM value and 95th percentile CT attenuation value and fifth percentile QSM value: 0.38 [$P = .009$] and 0.34 [$P = .01$], respectively) except for mean CT attenuation value and mean QSM of calcified lesions (Figs 6b, E3 [online]; Table 2). The slopes and root mean square error values of linear regression are also listed in Table 3. No significant correlations ($P < .05$) were identified in any other ROIs. The results of analysis of intraclass correlation coefficients are listed in Table E2 (online).

With regard to the analysis of healthy volunteers only, negative correlations were still observed in the choroid plexus (R^2 of mean CT attenuation value and mean QSM value, maximum CT attenuation value and minimum QSM value, and 95th percentile CT attenuation value and fifth percentile QSM value: 0.66, 0.53, and 0.54, respectively; $P < .001$). Weaker correlations were seen in the GP of healthy volunteers (R^2 of mean CT attenuation value and mean QSM value, maximum CT attenuation value and maximum QSM value, and 95th percentile CT attenuation value and 95th percentile QSM value: 0.19 [$P = .005$], 0.29 [$P < .001$], and 0.26 [$P < .001$], respectively) than in the results

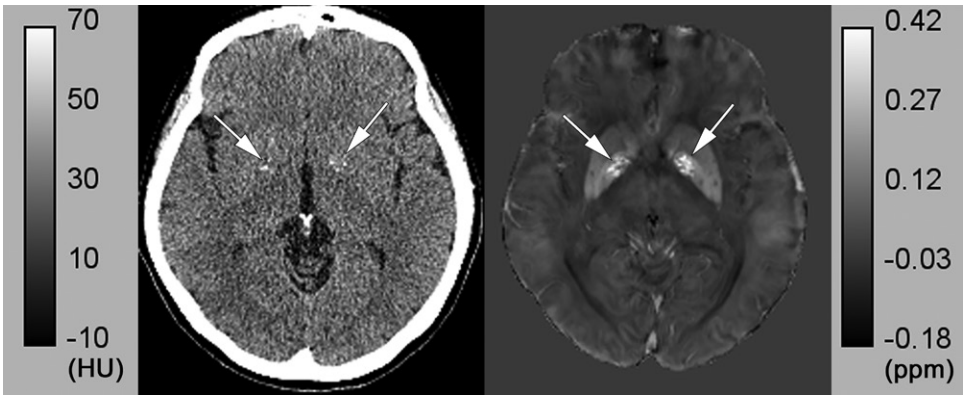

Figure 4: Images in 64-year-old healthy female volunteer. Paramagnetic metals such as iron accumulate in globus pallidus, accompanying calcification. Unenhanced CT image (left) shows high-attenuation spots in globus pallidus (arrows) that correspond to "physiologic calcification." Image from quantitative susceptibility mapping (right) shows high susceptibility (arrows) due to paramagnetic deposits such as iron.

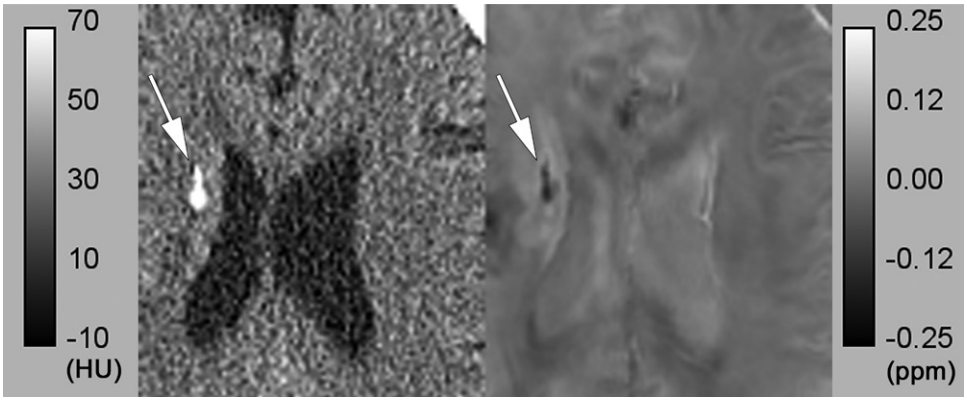

Figure 5: Images in 42-year-old man who underwent surgery and chemoradiation therapy for anaplastic astrocytoma. Unenhanced CT image (left) shows high-attenuation area in corona radiata (arrow). Image from quantitative susceptibility mapping (right) shows low susceptibility (arrow), which is suggestive of calcification.

for the total cohort (Fig E5 [online]). The correlation coefficients adjusted for age and interval between CT and MRI are listed in Table E3 (online). Coefficients of variation for ROIs in CT attenuation values and susceptibilities of healthy volunteers (n = 20), patients (n = 84), and the total cohort (n = 104) are shown in Table E4 (online).

Details of assessment of the diagnosis of lesions based on CT images are provided in Figure E6 (online).

Discussion

The phantom study demonstrated a positive correlation between gadolinium concentration and maximum CT attenuation values and maximum susceptibility (R^2 = 0.95 [$P < .001$] and 0.99 [$P < .001$], respectively) and calcium carbonate ($CaCO_3$) concentration and maximum CT attenuation values (R^2 = 0.89, P = .005). There was a negative correlation between $CaCO_3$ concentration and minimum susceptibility (R^2 = 0.98, $P < .001$). In the human study, we demonstrated a positive correlation between maximum CT attenuation values and maximum susceptibility in the globus pallidus (GP) (R^2 = 0.52, $P < .001$). No correlations were apparent in the putamen, caudate nucleus, red nucleus, substantia nigra, or dentate nucleus, in which regions the coefficients of variation of CT attenuation values were relatively low. In hemorrhagic lesions, a positive correlation was identified between maximum CT attenuation values and maximum susceptibility (R^2 = 0.38, $P < .001$) due to high CT attenuation values and high susceptibility of hemorrhage, but the correlation was still weaker than that in the GP. Negative correlations were seen between maximum CT attenuation values and minimum susceptibility in the choroid plexus and in calcified lesions (R^2 = 0.53 [$P < .001$] and 0.38 [P = .009]) due to the high CT attenuation values and negative susceptibility of calcification. The lower R^2 of calcified lesions compared with the choroid plexus may be caused by the difference in calcium compounds and proportion of calcium between pathologic calcification and calcification of the choroid plexus. In the 20 healthy volunteers, the correlation was strong in the choroid plexus but was weaker in the GP compared with that in the total cohort. The coefficients of variation of the CT attenuation values and susceptibility in the GP were lower in the healthy volunteers than in the patients. To our knowledge, this is the first study to assess correlations by using maximum (or minimum) and 95th percentile (or fifth percentile) values. In the GP and calcified lesions, R^2 values for the relationship between maximum CT attenuation value and maximum quantitative susceptibility mapping (QSM) value (or maximum CT attenuation value and minimum QSM value) and 95th percentile CT attenuation value and 95th percentile QSM value (or 95th percentile CT attenuation value and fifth percentile QSM value) were higher than those for mean CT attenuation value and mean QSM value and may reflect the characteristics of these areas better.

The basal ganglia (particularly the GP) are known to have high CT attenuation values owing to so-called "physiologic calcification" (19,20), which is accompanied by the deposition of various other metals (eg, zinc, iron, copper, manganese, and aluminum) (21). In fact, previous studies have revealed the GP to be the most iron-rich structure in the brain (13,16). Although calcium in the GP causes negative susceptibility with QSM, this may be overwhelmed by the strong paramagnetic property of iron (22) because QSM measures overall bulk magnetic

Table 2: CT Attenuation Values, Susceptibility Values, and Relationship between Them in Human Study

A: Paramagnetic ROIs

Structure and Parameter	Relationship between CT_{mean} and QSM_{mean}	Relationship between CT_{max} and QSM_{max}	Relationship between CT_{95th} and QSM_{95th}
Globus pallidus			
CT attenuation (HU)	34.5 ± 4.5	62.4 ± 16.8	50.2 ± 9.6
QSM value (ppm)	0.19 ± 0.07	0.32 ± 0.15	0.28 ± 0.13
Pearson correlation	*R*: 0.55, R^2: 0.30 (<.001)	*R*: 0.72, R^2: 0.52 (<.001)	*R*: 0.71, R^2: 0.50 (<.001)
Spearman correlation	*R*: 0.35, R^2: 0.12 (<.001)	*R*: 0.60, R^2: 0.36 (<.001)	*R*: 0.55, R^2: 0.30 (<.001)
Putamen			
CT attenuation (HU)	35.3 ± 2.5	55.6 ± 5.2	48.4 ± 3.1
QSM (ppm)	0.08 ± 0.04	0.16 ± 0.06	0.13 ± 0.05
Pearson correlation	*R*: 0.06, R^2: 0.003 (.41)	*R*: 0.06, R^2: 0.003 (.42)	*R*: 0.03, R^2: 0.001 (.66)
Spearman correlation	*R*: 0.03, R^2: 0.001 (.66)	*R*: 0.07, R^2: 0.005 (.32)	*R*: 0.01, R^2: 0.000 (.91)
Caudate nucleus			
CT attenuation (HU)	35.1 ± 2.6	54.7 ± 4.8	48.1 ± 3.3
QSM (ppm)	0.07 ± 0.03	0.14 ± 0.05	0.11 ± 0.05
Pearson correlation	*R*: −0.15, R^2: 0.02 (.03)	*R*: −0.06, R^2: 0.003 (.43)	*R*: −0.12, R^2: 0.02 (.08)
Spearman correlation	*R*: −0.19, R^2: 0.04 (.007)	*R*: −0.07, R^2: 0.005 (.35)	*R*: −0.11, R^2: 0.01 (.10)
Red nucleus			
CT attenuation (HU)	30.1 ± 3.4	46.3 ± 5.5	42.5 ± 4.2
QSM value (ppm)	0.11 ± 0.06	0.15 ± 0.07	0.14 ± 0.07
Pearson correlation	*R*: 0.03, R^2: 0.001 (.68)	*R*: −0.004, R^2: 0.000 (.96)	*R*: 0.02, R^2: 0.000 (.73)
Spearman correlation	*R*: 0.003, R^2: 0.000 (.97)	*R*: −0.06, R^2: 0.003 (.38)	*R*: −0.09, R^2: 0.008 (.19)
Substantia nigra			
CT attenuation (HU)	31.7 ± 3.4	48.4 ± 5.9	44.4 ± 4.8
QSM value (ppm)	0.15 ± 0.05	0.22 ± 0.08	0.21 ± 0.07
Pearson correlation	*R*: 0.10, R^2: 0.01 (.15)	*R*: 0.06, R^2: 0.004 (.35)	*R*: 0.08, R^2: 0.006 (.26)
Spearman correlation	*R*: 0.10, R^2: 0.01 (.16)	*R*: 0.05, R^2: 0.003 (.52)	*R*: 0.07, R^2: 0.005 (.33)
Dentate nucleus			
CT attenuation (HU)	31.1 ± 3.8	51.1 ± 5.9	44.6 ± 5.3
QSM value (ppm)	0.12 ± 0.05	0.17 ± 0.07	0.16 ± 0.06
Pearson correlation	*R*: 0.11, R^2: 0.01 (.12)	*R*: 0.18, R^2: 0.03 (.009)	*R*: 0.22, R^2: 0.05 (.002)
Spearman correlation	*R*: 0.12, R^2: 0.01 (.08)	*R*: 0.19, R^2: 0.04 (.006)	*R*: 0.17, R^2: 0.03 (.02)
Hemorrhagic lesions			
CT attenuation (HU)	37.4 ± 11.4	52.5 ± 15.8	49.0 ± 13.0
QSM value (ppm)	0.57 ± 0.30	0.73 ± 0.32	0.70 ± 0.31
Pearson correlation	*R*: 0.64, R^2: 0.41 (<.001)	*R*: 0.62, R^2: 0.38 (<.001)	*R*: 0.62, R^2: 0.38 (<.001)
Spearman correlation	*R*: 0.64, R^2: 0.41 (<.001)	*R*: 0.62, R^2: 0.38 (<.001)	*R*: 0.63, R^2: 0.40 (<.001)

B: Diamagnetic ROIs

Structure and Parameter	Relationship between CT_{mean} and QSM_{mean}	Relationship between CT_{max} and QSM_{min}	Relationship between CT_{95th} and QSM_{5th}
Choroid plexus			
CT attenuation (HU)	94.0 ± 54.6	139.0 ± 85.3	132.6 ± 79.2
QSM value (ppm)	−0.14 ± 0.08	−0.19 ± 0.10	−0.18 ± 0.10
Pearson correlation	*R*: −0.76, R^2: 0.58 (<.001)	*R*: −0.73, R^2: 0.53 (<.001)	*R*: −0.75, R^2: 0.56 (<.001)
Spearman correlation	*R*: −0.78, R^2: 0.61 (<.001)	*R*: −0.80, R^2: 0.64 (<.001)	*R*: −0.80, R^2: 0.64 (<.001)
Calcified lesions			
CT attenuation (HU)	377.0 ± 222.6	528.6 ± 340.0	510.5 ± 326.3
QSM value (ppm)	−0.26 ± 0.07	−0.32 ± 0.10	−0.30 ± 0.09
Pearson correlation	*R*: −0.38, R^2: 0.15 (.13)	*R*: −0.62, R^2: 0.38 (.009)	*R*: −0.59, R^2: 0.34 (.01)
Spearman correlation	*R*: −0.42, R^2: 0.18 (.09)	*R*: −0.56, R^2: 0.31 (.02)	*R*: −0.55, R^2: 0.30 (.02)

Note.—Unless otherwise specified, data are means ± standard deviations of CT attenuation values and susceptibility values. Numbers in parentheses are *P* values. CT_{max} = maximum CT attenuation value, CT_{mean} = mean CT attenuation value, CT_{95th} = 95th percentile CT attenuation value, QSM = quantitative susceptibility mapping, QSM_{max} = maximum QSM value, QSM_{mean} = mean QSM value, QSM_{min} = minimum QSM value, QSM_{5th} = fifth percentile QSM value, QSM_{95th} = 95th percentile QSM value, ROI = region of interest.

Figure 6: **(a)** Scatter plot shows maximum CT attenuation value (CT_{max}) and maximum quantitative susceptibility mapping (QSM_{max}) value for gadolinium (Gd) and calcium carbonate (Ca) phantoms, normal structures, and pathologic lesions in all patients and volunteers. Minimum QSM values was used instead of maximum QSM value for $CaCO_3$, choroid plexus, and calcified lesions. Globus pallidus (GP), putamen, caudate nucleus, red nucleus, substantia nigra, dentate nucleus, and hemorrhagic lesions are paramagnetic, whereas choroid plexus and calcified lesions are diamagnetic. **(b)** Scatter plots of CT_{max} and QSM_{max} in GP and hemorrhagic lesions (left column) and maximum CT attenuation value (CT_{max}) and minimum QSM value (QSM_{min}) in choroid plexus and calcified lesions (right column). Pink dots represent healthy volunteers. Linear regression analysis showed positive correlations between CT attenuation values and susceptibility in GP ($R^2 = 0.52$, $P < .001$) and hemorrhagic lesions ($R^2 = 0.38$, $P < .001$). Negative correlations are observed in choroid plexus ($R^2 = 0.53$, $P < .001$) and calcified lesions ($R^2 = 0.38$, $P = .009$). RMSE = root mean square error.

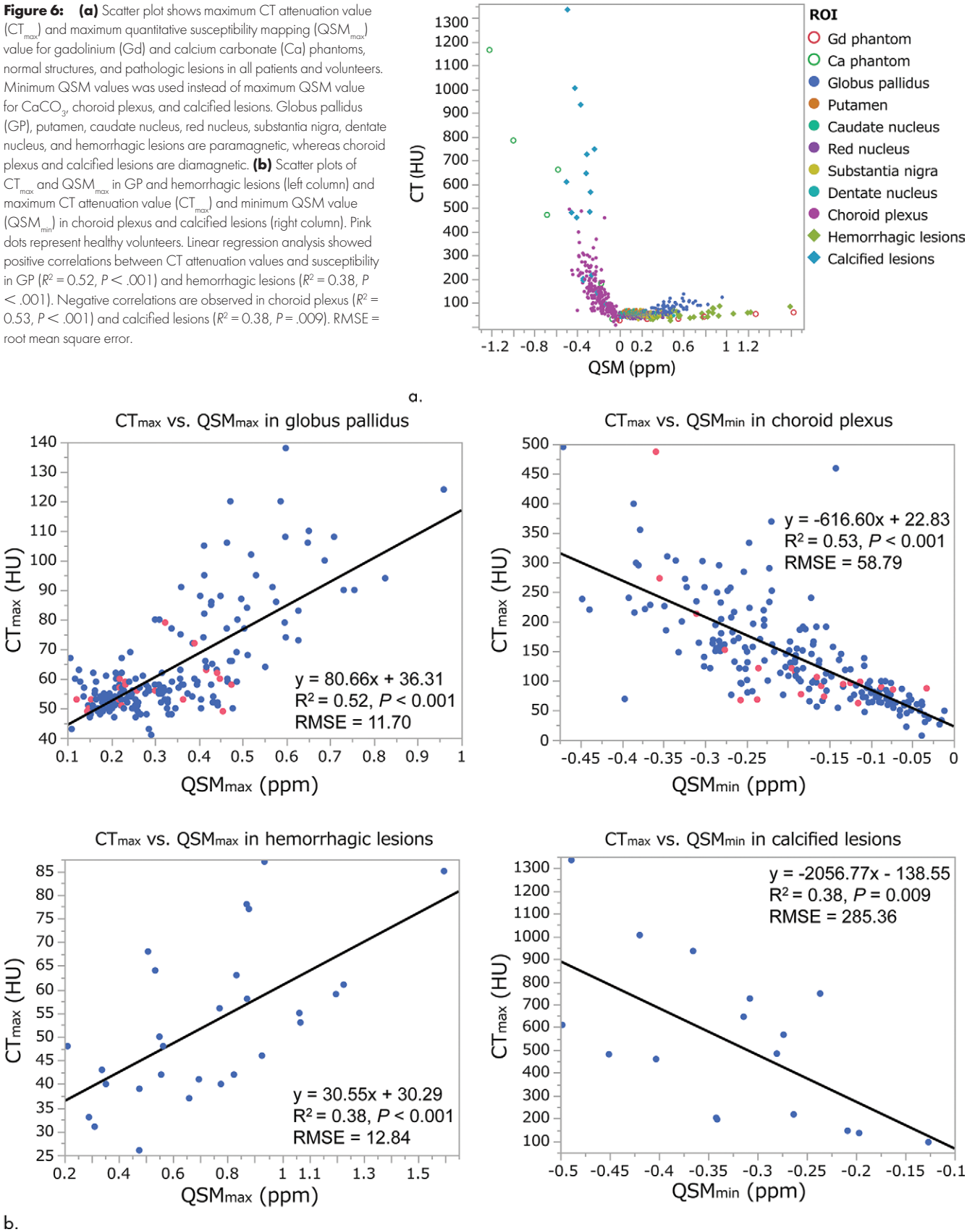

Table 3: Slope and Root Mean Square Error of Linear Regression between CT Attenuation Values and Magnetic Susceptibility

A: Paramagnetic ROIs			
Structure and Parameter	Relationship between CT_{mean} and QSM_{mean}	Relationship between CT_{max} and QSM_{max}	Relationship between CT_{95th} and QSM_{95th}
Globus pallidus			
Slope (HU/ppm)	37.23 (29.43, 45.02)	80.66 (70.00, 91.33)	52.22 (45.05, 59.39)
RMSE	3.79	11.70	6.78
Hemorrhagic lesions			
Slope (HU/ppm)	24.52 (12.58, 36.45)	30.55 (14.94, 46.17)	25.69 (12.59, 38.79)
RMSE	9.14	12.84	10.58
B: Diamagnetic ROIs			
Structure and Parameter	Relationship between CT_{mean} and QSM_{mean}	Relationship between CT_{max} and QSM_{min}	Relationship between CT_{95th} and QSM_{5th}
Choroid plexus			
Slope (HU/ppm)	−520.31 (−580.74, −459.88)	−616.60 (−696.36, −536.84)	−601.65 (−675.23, −528.08)
RMSE	35.48	58.79	52.93
Calcified lesions			
Slope (HU/ppm)	−1231.79 (−2863.50, 399.92)	−2056.77 (−3507.08, −606.46)	−2017.59 (−3553.43, −481.75)
RMSE	218.84	285.36	281.52

Note.—Numbers in parentheses are 95% confidence intervals. CT_{max} = maximum CT attenuation value, CT_{mean} = mean CT attenuation value, CT_{95th} = 95th percentile CT attenuation value, QSM = quantitative susceptibility mapping, QSM_{max} = maximum QSM value, QSM_{mean} = mean QSM value, QSM_{min} = minimum QSM value, QSM_{5th} = fifth percentile QSM value, QSM_{95th} = 95th percentile QSM value, RMSE = root mean square error, ROI = region of interest.

susceptibility. This might be the reason why our results showed a positive correlation between CT attenuation values and susceptibility in the GP. Our results also suggest that the amounts of calcification and iron deposition in the GP are correlated with each other, although pathologic assessments cannot be performed. The reason why the GP of healthy volunteers showed a weaker correlation than did the GP in the total cohort could be a lower abundance of iron deposits and calcification in this group, which would result in a narrower distribution of the CT attenuation values and QSM values.

Iron deposits have been reported in the putamen, caudate nucleus, red nucleus, substantia nigra, and dentate nucleus but are smaller than those in the GP (13,16); similarly, physiologic calcification is not often observed in these areas on CT images. We consider that the amounts of iron and calcium deposition at these sites are insufficient to produce a correlation between CT attenuation values and susceptibility.

We suggest that CT attenuation values can be estimated from susceptibility in those areas where significant correlations were observed between CT attenuation values and susceptibility (eg, GP, choroid plexus, and hemorrhagic and calcified lesions). We could potentially substitute MRI for CT in these areas. In structures where no significant correlation was found, an anatomic dependent constant value could potentially be used as an estimated CT attenuation value. However, more detailed assessment would be required.

Several limitations of our study must be considered. First, we excluded a large number of patients (because of an excessive interval between CT and QSM in 58 patients and poor image quality in five), which may have caused selection bias. In addition, in 81 of the 104 patients and volunteers (78%), CT and MRI were performed on different days. In most patients, underlying disease was chronically stable; however, lesion status may still have changed slightly during the time between imaging examinations. Second, we used several CT scanners and a 51%–80% reduced-dose CT protocol for the healthy volunteers. The difference in imaging parameters may have produced subtle differences in the CT attenuation values. However, the CT attenuation values are quantitative and have high reproducibility; because of the iterative approximation method used, we obtained good image quality even with lower-dose CT (23). Third, although the registration between CT and QSM images was reasonable and no difficulties were encountered in ROI placement, pixel-wise accuracy was not validated owing to the relatively low contrast in CT images of the brain. Fourth, we did not conduct tissue sample analyses such as mass spectrometry or histologic study. Only three lesions were confirmed at histopathologic examination. Calcification may have contained calcium phosphate and other substances (24), but no composition analysis was available. Fifth, a variety of hemorrhagic and calcified lesions were included in our patient cohort, which may have led to relatively dispersed plots. Sixth, we did not calibrate susceptibility values with the cerebrospinal fluid space or white matter (25). Although a previous study reported a proper zero reference for brain QSM to force cerebrospinal fluid to zero during QSM reconstruction (26), the ventricles and white matter can often appear highly heterogeneous at QSM and can alter during aging (27,28) and in a cohort with disease, and therefore may be unreliable as references. Last, streaking artifacts are seen in some images in this study. The MEDI+0 automatic zero referencing program (26) has the potential to remove these artifacts by enforcing homogeneity in specified regions.

In conclusion, positive correlations between CT attenuation values and susceptibility were observed in the globus pallidus and hemorrhagic lesions, and negative correlations were found in the choroid plexus and calcified lesions. Our results suggest the possibility of estimating CT attenuation values from quantitative susceptibility mapping; however, further studies focusing on different diseases are needed to better comprehend the relationship between CT attenuation values and magnetic susceptibility.

Acknowledgments: We are grateful to Katsutoshi Murata, MSc, and Yuta Urushibata, MSc, Siemens Healthcare K. K., for protocol optimization.

Author contributions: Guarantors of integrity of entire study, S.O., Y.F., Y.A., K. Togashi; study concepts/study design or data acquisition or data analysis/interpretation, all authors; manuscript drafting or manuscript revision for important intellectual content, all authors; approval of final version of submitted manuscript, all authors; agrees to ensure any questions related to the work are appropriately resolved, all authors; literature research, S.O., Y.F., C.L., Y.A., N.S.; clinical studies, S.O., Y.F., T.O., Y.Y., Y.A., N.S., K. Togashi; experimental studies, Y.F., K. Takakura, Y.A., N.S.; statistical analysis, S.O., Y.F., T.O., Y.A., N.S.; and manuscript editing, S.O., Y.F., T.O., C.L., Y.A., N.S., S.M., K. Togashi

Disclosures of Conflicts of Interest: S.O. disclosed no relevant relationships. **Y.F.** disclosed no relevant relationships. **T.O.** Activities related to the present article: disclosed no relevant relationships. Activities not related to the present article: institution has a research grant from Siemens Healthcare K.K.; institution received payment for lectures including service on speakers bureaus from Siemens Healthcare. **K.K.** Other relationships: disclosed no relevant relationships. **K. Takakura** disclosed no relevant relationships. **C.L.** Activities related to the present article: disclosed no relevant relationships. Activities not related to the present article: disclosed no relevant relationships. Other relationships: has a patent issued. **Y.Y.** disclosed no relevant relationships. **Y.A.** Activities related to the present article: disclosed no relevant relationships. Activities not related to the present article: institution has research grants from Siemens, Philips, Sanofi, Nihon Medi-Physics, Brainlab, Zeiss, TanabeMitsubishi, Chugai, Eisai, Merck, Meiji Seika, Daiichi Sankyo, CLS, Takeda, and Pfizer; receives payment for lectures including service on speakers bureaus from NipponKayaku, Chugai, Eisai, Merck, MeijiSeika, Otsuka, Brainlab, Daiichi Sankyo, UCB, Novocure, Abbvie, and CSL Behring. Other relationships: disclosed no relevant relationships. **N.S.** disclosed no relevant relationships. **S.M.** disclosed no relevant relationships. **K. Togashi** disclosed no relevant relationships.

References

1. Go JL, Zee CS. Unique CT imaging advantages. Hemorrhage and calcification. Neuroimaging Clin N Am 1998;8(3):541–558.
2. Nute JL, Le Roux L, Chandler AG, Baladandayuthapani V, Schellingerhout D, Cody DD. Differentiation of low-attenuation intracranial hemorrhage and calcification using dual-energy computed tomography in a phantom system. Invest Radiol 2015;50(1):9–16.
3. Liu C, Li W, Tong KA, Yeom KW, Kuzminski S. Susceptibility-weighted imaging and quantitative susceptibility mapping in the brain. J Magn Reson Imaging 2015;42(1):23–41.
4. Shmueli K, de Zwart JA, van Gelderen P, Li TQ, Dodd SJ, Duyn JH. Magnetic susceptibility mapping of brain tissue in vivo using MRI phase data. Magn Reson Med 2009;62(6):1510–1522.
5. Schweser F, Deistung A, Lehr BW, Reichenbach JR. Differentiation between diamagnetic and paramagnetic cerebral lesions based on magnetic susceptibility mapping. Med Phys 2010;37(10):5165–5178.
6. Wang Y, Liu T. Quantitative susceptibility mapping (QSM): decoding MRI data for a tissue magnetic biomarker. Magn Reson Med 2015;73(1):82–101.
7. Li W, Wu B, Liu C. Quantitative susceptibility mapping of human brain reflects spatial variation in tissue composition. Neuroimage 2011;55(4):1645–1656.
8. Sun H, Klahr AC, Kate M, et al. Quantitative Susceptibility Mapping for Following Intracranial Hemorrhage. Radiology 2018;288(3):830–839.
9. de Rochefort L, Liu T, Kressler B, et al. Quantitative susceptibility map reconstruction from MR phase data using bayesian regularization: validation and application to brain imaging. Magn Reson Med 2010;63(1):194–206.
10. Hinoda T, Fushimi Y, Okada T, et al. Quantitative Susceptibility Mapping at 3 T and 1.5 T: Evaluation of Consistency and Reproducibility. Invest Radiol 2015;50(8):522–530.
11. Tan H, Liu T, Wu Y, et al. Evaluation of iron content in human cerebral cavernous malformation using quantitative susceptibility mapping. Invest Radiol 2014;49(7):498–504.
12. Bilgic B, Pfefferbaum A, Rohlfing T, Sullivan EV, Adalsteinsson E. MRI estimates of brain iron concentration in normal aging using quantitative susceptibility mapping. Neuroimage 2012;59(3):2625–2635.
13. Langkammer C, Schweser F, Krebs N, et al. Quantitative susceptibility mapping as a means to measure brain iron? A post mortem validation study. Neuroimage 2012;62(3):1593–1599.
14. Zhang Y, Wei H, Sun Y, et al. Quantitative susceptibility mapping (QSM) as a means to monitor cerebral hematoma treatment. J Magn Reson Imaging 2018;48(4):907–915.
15. Wang S, Lou M, Liu T, Cui D, Chen X, Wang Y. Hematoma volume measurement in gradient echo MRI using quantitative susceptibility mapping. Stroke 2013;44(8):2315–2317.
16. Hallgren B, Sourander P. The effect of age on the non-haemin iron in the human brain. J Neurochem 1958;3(1):41–51.
17. Chen W, Zhu W, Kovanlikaya I, et al. Intracranial calcifications and hemorrhages: characterization with quantitative susceptibility mapping. Radiology 2014;270(2):496–505.
18. Nakajima S, Okada T, Yamamoto A, et al. Primary central nervous system lymphoma and glioblastoma: differentiation using dynamic susceptibility-contrast perfusion-weighted imaging, diffusion-weighted imaging, and (18)F-fluorodeoxyglucose positron emission tomography. Clin Imaging 2015;39(3):390–395.
19. Adams AE. Basal ganglia calcification. Characteristics of CT scans and clinical findings. Neurosurg Rev 1980;3(3):201–203.
20. Wagner JA, Slager UT, Dennis JM, Barnes EV. The incidence and composition of radiopaque deposits in the basal ganglia of the brain. Am J Roentgenol Radium Ther Nucl Med 1955;74(2):232–234.
21. Atlas SW, Grossman RI, Hackney DB, et al. Calcified intracranial lesions: detection with gradient-echo-acquisition rapid MR imaging. AJR Am J Roentgenol 1988;150(6):1383–1389.
22. Bartzokis G, Aravagiri M, Oldendorf WH, Mintz J, Marder SR. Field dependent transverse relaxation rate increase may be a specific measure of tissue iron stores. Magn Reson Med 1993;29(4):459–464.
23. Korn A, Fenchel M, Bender B, et al. Iterative reconstruction in head CT: image quality of routine and low-dose protocols in comparison with standard filtered backprojection. AJNR Am J Neuroradiol 2012;33(2):218–224.
24. Bazin D, Daudon M, Combes C, Rey C. Characterization and some physicochemical aspects of pathological microcalcifications. Chem Rev 2012;112(10):5092–5120.
25. Deistung A, Schweser F, Reichenbach JR. Overview of quantitative susceptibility mapping. NMR Biomed 2017;30(4):e3569.
26. Deh K, Kawaji K, Bulk M, et al. Multicenter reproducibility of quantitative susceptibility mapping in a gadolinium phantom using MEDI+0 automatic zero referencing. Magn Reson Med 2019;81(2):1229–1236.
27. Zhang Y, Wei H, Cronin MJ, He N, Yan F, Liu C. Longitudinal atlas for normative human brain development and aging over the lifespan using quantitative susceptibility mapping. Neuroimage 2018;171:176–189.
28. Zhang Y, Shi J, Wei H, Han V, Zhu WZ, Liu C. Neonate and infant brain development from birth to 2 years assessed using MRI-based quantitative susceptibility mapping. Neuroimage 2019;185:349–360.